ANNALS OF GEOPHYSICS, 61, 6, SUP; VO671, 2018; doi: 10.4401/ag-7865

"PARTICLE SHAPE ANALYZER PARTISAN – AN OPEN SOURCE TOOL FOR MULTI-STANDARD TWO-DIMENSIONAL PARTICLE MORPHOMETRY ANALYSIS"

Tobias Dürig*,[1], M. Hamish Bowman[1], James D. L. White[1], Arran Murch[1], Daniela Mele[2], Andrea Verolino[21], Pierfrancesco Dellino[2]

(1) Geology Department, University of Otago, Dunedin, New Zealand
(2) Dipartimento di Scienze della Terra e Geoambientali, Università degli studi di Bari Aldo Moro

Article history
Receveid July 30, 2018; accepted September 11, 2018.
Subject classification:
Morphometry; Volcanic ash; Image particle analysis; IPA; Tephra; Grain; Shape parameters.

ABSTRACT

Volcanic particles are commonly characterized using 2D morphometric analysis. Results of analysis are used to compare particles from different events or phases, and to infer clast-generating mechanisms, eruptive styles and the aerodynamic behavior of particles. Such particle-shape analyses can be made from images of particle silhouettes or cross-sectional slices. A number of different morphometric systems have been used to date, with each using its own nomenclature and mathematical definitions of shape-describing parameters. Some of the parameters can only be obtained using specific commercial software.

With the PARTIcle Shape ANalyzer PARTISAN we present a freeware tool which parameterizes 2D shapes and provides a suite of shape parameters, following the different standards of the five most commonly used 2D morphometric systems. PARTISAN enables the user to study and archive the results of particle-shape analysis in a format compatible with various published routines, thus increasing the potential for linking new work with results of work previously published by other groups. It will also allow cross-comparison of results obtained by different morphological routines. We see PARTISAN as a "Rosetta Stone" for volcanological particle morphometry, and it opens the way for development of widely agreed treatment of particle shapes in 2D.

1. INTRODUCTION

The only record of many volcanological processes and events is held in their erupted products. Among the features of volcanic particles (e.g. geochemistry, glass-volatile content, vesicularity, crystal morphology), it is the shapes of particles, including their fine-scale surface features, that most directly reflect the fragmentation processes that formed them [Heiken, 1972, 1974; Heiken and Wohletz, 1985; Cioni et al., 1992; Büttner et al., 1999].

Virtually all studies of pyroclastic deposits include some description of particle shapes, but there has been limited progress toward a consistent and interpreter-independent method of characterizing particle shapes. Some tools have been developed that normalize for size effects and characterize the projected shapes of ash particles in two dimensions in a procedure which is commonly known as 2D morphometry. One of the most commonly used morphometric systems was introduced to volcanology by Dellino and La Volpe [1996], who

suggested a classification scheme using four shape parameters acquired from 2D binarized particle images (silhouettes) produced by projection of 3D shapes. The "Image Particle shape Analysis" (IPA) parameters were measured by Dellino and La Volpe [1996] from high-resolution scanning electron microscope (SEM) images, and the IPA parameterization has been used in multiple studies to either compare tephra grains from different eruptions, or to compare products of different eruptive phases [Heiken, 1974; Dellino et al., 2001; Taddeucci and Palladino, 2002; Cioni et al., 2008; Murtagh and White, 2013; Iverson et al., 2014; Alvarado et al., 2016]. Other studies have used characteristics of particles generated by known processes in fragmentation experiments to infer the processes that generated natural tephra particles during eruptions [Büttner et al., 2002; Dürig et al., 2012; Schipper et al., 2013; Jordan et al., 2014]. Others have studied fallout ash during ongoing eruptions using semi-automated routines [Lautze et al., 2012, 2013], and have derived aerodynamic properties of ash grains relevant to their dispersal and sedimentation [Mele et al., 2011].

In addition to the method introduced by Dellino and La Volpe [1996], a multitude of other shape parameterization approaches have been presented and applied. Some focus on analyzing transport processes in volcanic plumes [Riley et al., 2003; Durant et al., 2009; Klawonn et al., 2014], others seek to determine magma discharge rates and eruption dynamics [Yamanoi et al., 2008; Wright et al., 2012; Miwa et al., 2013, 2015; Suzuki et al., 2013; Eychenne et al., 2015] or reconstruct eruptive mechanisms [Cioni et al., 2008, 2014; Liu et al., 2015b; Schmith et al., 2017]. Descriptive parameters have also been introduced which can be provided by automated procedures, suitable for real-time, surveillance of eruptions [Leibrandt and Le Pennec, 2015].

2. CHALLENGES FOR COMPARING SHAPE PARAMETERS FROM DIFFERENT MORPHOLOGICAL SYSTEMS

A key objective in particle shape analysis is to identify specific characteristics of grain shapes that record specific volcanic processes (e.g. the fragmentation mechanism). The scientific impact of a study is greatly increased if the morphometric results can be directly compared with those already published from other samples.

Such comparisons are currently difficult for several reasons. First, it is important to note that image resolution will strongly affect the outcome of any morphometric analysis - especially the perimeter of the analyzed object, and all derived shape parameters based on that metric [Dellino and La Volpe, 1996; Liu et al., 2015a; Schmith et al., 2017]. Care has therefore to be taken that the compared morphometric results are based on images with comparable resolution and magnification (requiring the user to study similar grain sizes). For the same reason, shape parameters derived from pictures obtained by different techniques, such as by optical microscopy or by SEM, cannot be directly compared.

Further complications arise from the fact that morphometric studies have applied two fundamentally different methods of particle preparation. One is the silhouette-based 2D analysis, for which particles are mounted on e.g. a carbon-tape. The other uses polished thin sections or polished grain mounts. This has the significant advantages of being also applicable to lithified samples, and in providing information about internal features of the particles (e.g. vesicle abundance and size distribution; microlites and phenocrysts) [Cioni et al., 2014], but the 2D grain shape from a cut section is not the same as the 2D projection (silhouette) from a whole grain. The biggest shortcoming in this respect is that a cut section need not intersect any of the defining particle diameters – a cut that catches only one tip of a particle both underrepresents even the minimum diameter, and may misrepresent particle shape.

Results based on these two different approaches (silhouette vs slices) are incompatible, and no conversion from one to the other is possible. A silhouette's area will always be at least that of the largest area possible for any slice taken normal to the silhouette viewing axis, and may be many times larger. No other general statement can be made about the relationship of one slice to a silhouette along the same axis, and there is an infinite number of possible orientations for either slices or silhouettes for any particle.

Another major problem for comparability is that many of the shape parameters reported in literature have their own nomenclature and mathematical definitions, which overlap with previously defined ones in ways that can be misleading. For example, "circularity" is defined by Dellino and La Volpe [1996] as one of the four IPA parameters. Presumably to adjust the parameter so that the most-circular objects have the highest circularity value, Leibrandt and Le Pennec [2015] inverted

		Figure 1	Reference
p	particle perimeter	(a)	
A	projected area of particle	(a)	
w	width (short side of the minimum area bounding rectangle)	(a)	[Dürig et al. 2012]
b	breadth (long side of the minimum area bounding rectangle)	(a)	[Dürig et al. 2012]
c	perimeter of the circle with area A, hence: $c=2\sqrt{A\pi}$	(a)	[Dellino and La Volpe 1996]
d_H	Heywood diameter (diameter of a circle with area A) $d_H=2\sqrt{A/\pi}=\sqrt{2}\cdot c/\pi$	(a)	[Riley et al., 2003]
a	maximum intercept, i.e. longest segment inside a particle, parallel to the long side of the bounding rectangle	(b)	[Dürig et al. 2012]
m	mean intercept perpendicular to a	(b)	[Dürig et al., 2012]
L_b	length defined by the maximum length of all possible lines from one point of the perimeter to another point on the perimeter projected on the major axis of the particle (i.e., axis of minimum rotational energy).	(d)	[Leibrandt and Le Pennec 2015]
W_b	maximum of all possible lines from one point of the perimeter to another point on the perimeter, projected on the minor axis	(d)	[Leibrandt and Le Pennec 2015]
p_{cp}	perimeter of smallest convex polygon around particle	(a)	[Leibrandt and Le Pennec 2015]
A_{cp}	area of smallest convex polygon around particle	(a)	[Liu et al. 2015a]
e_{ce}	perimeter the smallest area ellipse that encloses, but does not intersect the particle	(c)	[Cioni et al. 2014]
L_{maj}	major axis of best fit ellipse	(c)	[Cioni et al. 2014]
L_{min}	minor axis of best fit ellipse	(c)	[Cioni et al. 2014]
d_{BC}	diameter of circle that encloses, but not intersects particle	(a)	[Schmith et al. 2017]
l_F	minimum Feret length (smallest distance between two parallel lines that contact but do not intersect particle);	(a)	[Schmith et al. 2017]
w_F	Feret length perpendicular to lF; identical to b	(a)	[Schmith et al. 2017]
d_F	maximum Feret distance (maximum distance between two parallel lines that contact but do not intersect particle)	(c)	

TABLE 1. Notation of basic metrics, computed by PARTISAN. For illustration, see Figure 1.

the equation but use the same name. For a parameter with the same name of "circularity", entirely different equations are used by Cioni et al. [2014], and Schmith et al. [2017]. Similarly problematic, the parameter "convexity" used by Schmith et al. [2017] is identical to the parameter called "solidity" by Liu et al. [2015a, 2015b],

whereas "rectangularity" as defined by Schmith et al. [2017] is identical to "compactness" in the notation of Dellino and La Volpe [1996]. In a different kind of inconsistency, "convexity", introduced by Liu et al. [2015a], uses the perimeter of the convex hull, whereas in the definition of Cioni et al. [2014], it is defined by the perimeter of the fitting ellipse. These are just a few examples of inconsistencies that make it challenging to compare results obtained from different studies. Applying the notation listed in Table 1, Table 2 gives an overview of the diversity of notations and mathematical definitions for five shape parameter concepts frequently used in volcanology. For a broader overview see Leibrandt and Le Pennec [2015] (their Table 3). One of the reasons for this apparent lack of standardization is the fact that different instruments and/or software have been used by different research groups, and the results impose their own terminology and measurement routines, which may not be reproducible on other machines or, when insufficiently documented, by any means.

In some cases [Leibrandt and Le Pennec, 2015; Schmith et al., 2017] software programs linked to the particle imaging system are used to obtain the shape parameters, so the authors used the terminology of the system. Other studies attempting to optimize shape parameters have had a specific focus on particular characteristics of volcanic particles, and have provided different suggestions for which shape parameters are best to use [Liu et al., 2015a; Schmith et al., 2017]. Although the advantages of a standardized morphological parameterization protocol are apparent, it is very likely that an agreed protocol could only be developed through the common agreement of a focused international commission; no such protocol has yet emerged [Gurioli et al., 2015]. But even if a generally accepted standard is accepted by large parts of the volcanology community, we would still face the problem that the morphometric work previously done might be impossible to rigorously compare with the new data. This would be a setback, blocking utilization of data archives painstakingly acquired over more than two decades.

To make a first step towards unifying the morphometric parameterization systems, a platform-independent, multi-standard tool is needed. We have developed such an open-source software tool, which we call PARTicle Shape ANalyzer (PARTISAN). It computes a multitude of shape parameters, and can reproduce most of the various morphometric analyses that have been presented in recent volcanological literature.

3. WHY PARTISAN?

PARTISAN supports the scientific method's requirement that results should be reproducible, and does so without any need for all researchers to employ a single "black-box" proprietary solution related to a device's operation.

Table 3 presents a list of studies on particles from more than 30 different sampling sites that have been morphometrically analyzed based on the IPA parameter concept by Dellino and La Volpe [1996]. They involve the investment of many hundreds of working hours. The IPA measurements, however, are made with commercial software, which makes it very difficult -if not impossible- for researchers who have no access to the program to obtain comparable parameters [Schmith et al., 2017]. PARTISAN addresses this problem.

1. It is independent from commercial hard- or software other than MATLAB™. Our open source script computes morphometric parameters using the IPA shape parameter system [Dellino and La Volpe, 1996]. Once IPA imaging guidelines are met, the user is guaranteed to obtain shape parameters compatible with those obtained by other groups using the IPA system, and with published results from it (see Table 3).
2. A multitude of shape parameters in addition to those of the original IPA [Dellino and La Volpe, 1996] are also obtained, using the specifications of morphometric analysis published by Cioni et al. [2014], Leibrandt and Le Pennec [2015], Liu et al. [2015a, 2015b] and Schmith et al. [2017].
3. The multi-standard output allows a PARTISAN user to compare shape-analysis data broadly, beyond the limitations imposed by any single specific group's standard. This approach also allows the PARTISAN user to find, for a given task, the shape parameter system most suitable for data interpretation.
4. The open source code allows continued peer-review and improvements by the volcanology community.

4. MORPHOMETRIC PARAMETERS OBTAINED BY PARTISAN

In addition to basic metrics (given in Table 1 and illustrated in Figure 1), PARTISAN provides shape parameters grouped into five morphometric systems, described below. All morphometric parameters are mathematically laid out in Table 2.

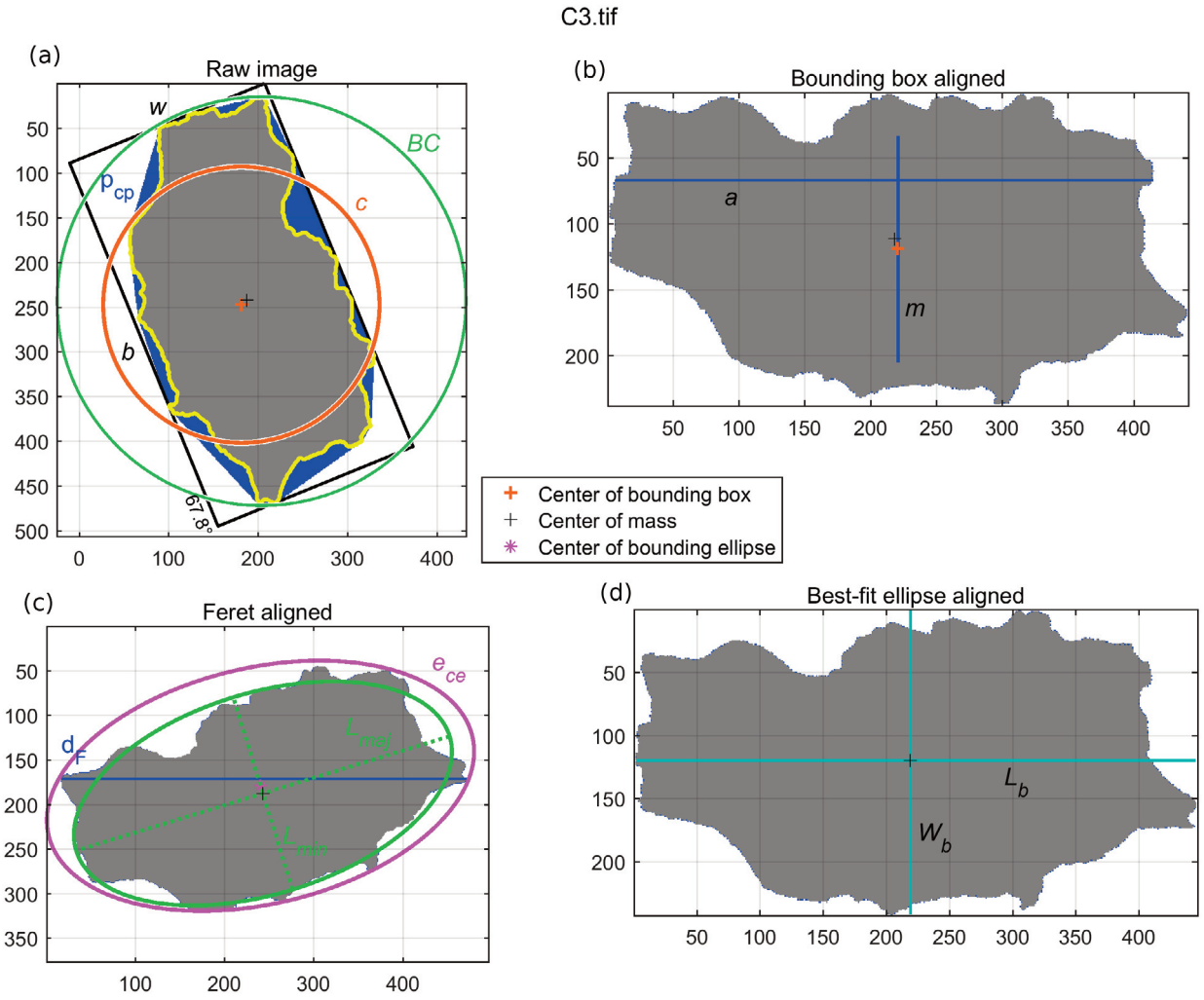

FIGURE 1. Screenshot of resulting figure provided by PARTISAN. See Table 1 for the description of annotated parameters. The analyzed particle is displayed in four orientations: (a) original orientation of the raw image; (b) particle rotated to the longer axis of the minimum bounding box; (c) orientated along the maximum Feret distance d_F (blue line); lines in green denote the major and minor axis of the best fit ellipse; (d) particle rotated to the major axis of the best-fit ellipse. The Feret lengths l_F and w_F listed in Table 1 are identical with the width w and breadth b of the minimum area bounding box displayed in (a). Also in (a), the particle perimeter p is highlighted in yellow. The perimeter p_{cp} is that of the smallest convex hull with area A_{cp}, which is illustrated in blue in the background of the grain silhouette. The diameter of the bounding circle denoted BC (in green) is listed in Table 1 as d_{BC}. The orange colored circle is of perimeter c and Heywood diameter d_H.

4.1 THE IPA PARAMETERS, BY DELLINO AND LA VOLPE [1996]

The image particle analysis ("IPA") parameter scheme of Dellino and La Volpe [1996] is probably the most established one, and most commonly used for morphometric analysis in volcanology; it is predominantly used to quantify the shapes of particle projections in SEM images, but also applied to optically derived silhouettes of particles and to SEM derived thin sections (see Table 3). It is described here in some detail in order to clarify several misunderstandings which have appeared over the years.

The first two IPA parameters (see also Table 2) are *circularity* $Circ_{DL}$, and *rectangularity* Rec_{DL}, with the latter depending on the minimum rectangle circumscribing the particle. It is important to note that the orientation of the minimum bounding rectangle is not fixed, and hence independent of the particle's orientation; this contrasts with the approach used in some freely available software, e.g. ImageJ [Schneider et al., 2012; Liu et al., 2015a], in which the bounding rectangle is constrained to have horizontal and vertical axes, regardless of how an elongate particle is oriented.

The other two IPA parameters are *compactness* Com_{DL} and *elongation* Elo_{DL}. The latter IPA parameter is defined as a fraction, with the longest segment in an

	Dellino and La Volpe [1996]	Cioni et al. [2014]	Leibrandt and Le Pennec [2015]	Liu et al. [2015a]	Schmith et al. [2017]
remarks	introduced as "IPA parameters", applied for discrimination between eruption types [1,2]	used to study tephra from Eyjafjallajökull 2010	used for in-situ measurements during eruptions	applied for studying the role of bubbles in phreato-magmatic eruptions[3]	applied for discrimination between eruption types
image acquisition method[4]	predominantly SEM silhouettes[5]	SEM silhouettes	automated optical projection silhouettes (Morphologi Optical Particle Analyzer, OPA)	SEM slices	automated optical projection silhouettes (Particle Insight dynamic shape analyzer, PIdsa)
software used to calculate parameters	ObtiLab	ImageJ	Associated Malven software	ImageJ	PIdsa
circularity	$Circ_{DL} = \frac{p}{c}$	$Circ_{cl} = \frac{4\pi A}{p^2}$	$Circ_{LL} = \frac{c}{p}$		$Circ_{SC} = \frac{4A}{\pi d_{BC^2}}$
rectangularity	$\mathrm{Re}c_{DL} = \frac{p}{2b+2w}$				$\mathrm{Re}c_{SC} = \frac{A}{b \cdot w}$
compactness	$Com_{DL} = \frac{A}{b \cdot w}$				
elongation	$Elo_{DL} = \frac{a}{m}$		$Elo_{LL} = 1 - \frac{W_b}{L_b}$		
form factor				$FF = \frac{4\pi A}{p^2}$	$FF = \frac{4\pi A}{p^2}$
ellipse aspect ratio		$AR_{Cl} = \frac{L_{maj}}{L_{\min}}$			
aspect ratio			$AR_{LL} = \frac{W_b}{L_b}$		
axial ratio				$AR_{LI} = \frac{L_{\min}}{L_{maj}}$	
Feret aspect ratio					$AR_F = \frac{l_F}{W_F}$ $AR_{SC} = \frac{W_F}{l_F}$
CE diameter			d_H		
convexity		$Con_{CL} = \frac{e_{ce}}{p}$	$Con_{LL} = \frac{p_{CP}}{p}$	$Con_{LI} = \frac{p_{CP}}{p}$	
solidity		$Sol_{Cl} = \frac{A}{A_{CP}}$	$Sol_{LL} = \frac{A}{A_{CP}}$	$Sol_{LI} = \frac{A}{A_{CP}}$	
regularity parameter					$\mathrm{Re}g = \frac{16A^3}{b \cdot w \cdot p^2 \cdot d_{BC^2}}$

TABLE 2. Morphometric systems and definition of respective shape parameters, provided by PARTISAN.
[1] using the notation of Dürig et al. [2012];
[2] List for studies using these IPA parameters: see Table 3;
[3] defined as "hydromagmatic" in Liu et al. [2015b, 2017]
[4] SEM stands for scanning electron microscope
[5] but also used to analyze SEM slices and silhouettes from both photographs and images obtained by optical microscopy. See Table 3 for detailed list.

object *parallel to the long side of the minimum rectangle circumscribing it* (denoted as "maximum intercept") as numerator, and the mean length of all chords with 1 pixel spacing perpendicular to the maximum intercept as denominator [Dürig et al., 2012]. We note that the definition of the maximum intercept is NOT identical with the maximum Feret diameter, but, probably because of an unclear description in the original paper by Dellino and La Volpe [1996], it is often misleadingly confused with it.

The four IPA parameters as introduced by the developers are provided by the commercial software Optilab Pro 2.6.1 from Graftek. The complicated definition of Elo_{DL} makes it, unfortunately, very difficult to adapt the IPA scheme for use without that software. We know of no available open source software available that computes the maximum and mean intercept according to the definition provided above. As a consequence, some studies using the IPA scheme without having access to Optilab, had to sidestep this problem, and did so by introducing other measures as replacement for Elo_{DL} (e.g., Schmith et al., 2017). We note that such a deviation from the original IPA scheme can still provide useful insights on how elongated the analyzed particles are. Results based on these "modified" elongation parameters are still comparable to data sets acquired by the same method, but they are not quantitatively comparable to those obtained by applying the "original" IPA scheme. In the future, by means of PARTISAN, researchers need no longer face this problem. All results computed by the open-source program will be comparable to the original IPA parameters provided by Optilab so long as the same protocol is followed for SEM image acquisition (see section 5.3), which is necessary to avoid introducing resolution-dependent differences in the quantitative results.

4.2 SHAPE PARAMETERS BY CIONI ET AL. [2014]

Cioni et al. [2014] morphometrically analyzed particles in the 0 ϕ fraction (1 to 1.4 mm) to characterize particles from different phases of the Eyjafjallajökull 2010 eruption.

They introduced four shape parameters (see Table 2): *solidity* Sol_{CI}, *convexity* $Conv_{CI}$, *circularity* $Circ_{CI}$ and ellipse *aspect ratio* AR_{CI}. These parameters were obtained using the public domain program ImageJ and binarized images from SEM [Schneider et al., 2012] of whole particles (silhouettes). After SEM analysis, the grains were sectioned, from which vesicle population and microlite data were acquired. The clasts analyzed had compositions ranging from benmorite to trachyte. The authors found that different eruptive styles produced different grain shapes, independent of the compositional changes.

4.3 SHAPE PARAMETERS BY LEIBRANDT AND LE PENNEC [2015]

This morphometric system was introduced to allow rapid automated measurements of 2D shapes projected from grains (i.e. silhouettes) by employing diascopic light imaging, and using a specialized optical particle analyzer "morpho-grainsizer" and associated software (Morphologi G3SE™ by Malvern Instruments™). It can be used for near real-time characterization of tephra during eruptive events. The suggested shape parameters include *circularity* $Circ_{LL}$, *aspect ratio* AR_{LL}, *convexity* $Conv_{LL}$ and *solidity* Sol_{LL} (see Table 2). The authors demonstrated their morphometric system on andesitic clasts from Tungurahua volcano, Ecuador, in the 250 -300 μm grain size range, produced by different eruption styles.

Of these parameters, the aspect ratio, as defined by Leibrandt and Le Pennec [2015], cannot be readily calculated without having a detailed description of the method used by the software, or access to the source code.

4.4 SHAPE PARAMETERS BY LIU ET AL. [2015A]

This scheme was originally developed to examine the role of bubbles in producing ash by phreatomagmatic ("hydromagmatic" by the authors) fragmentation. Unlike silhouette-based 2D analysis, this method is applied to 2D shapes from polished thin sections or polished grain mounts imaged with an SEM. For this purpose, four parameters were suggested for optimal particle shape description: form factor (which is equal to $Circ_{CI}$), *axial ratio* AR_{LI} (equal to the inverse of AR_{CI}), *convexity* $Conv_{LI}$ and *solidity* Sol_{LI} equivalent to $Conv_{LL}$ and solidity Sol_{LL}, respectively. These shape parameters have been applied, e.g. to study basaltic grains from Grímsvötn 2011 in four size fractions ranging from < 32 μm to 125 μm [Liu et al., 2015b].

4.5 SHAPE PARAMETERS USED BY SCHMITH ET AL. [2017]

This morphometric system was tailored to the particle shape analysis of bulk samples using the commercial Particle Insight™ dynamic shape analyzer (PIdsa), and associated software. This method works through automated optical acquisition of particle silhouettes.

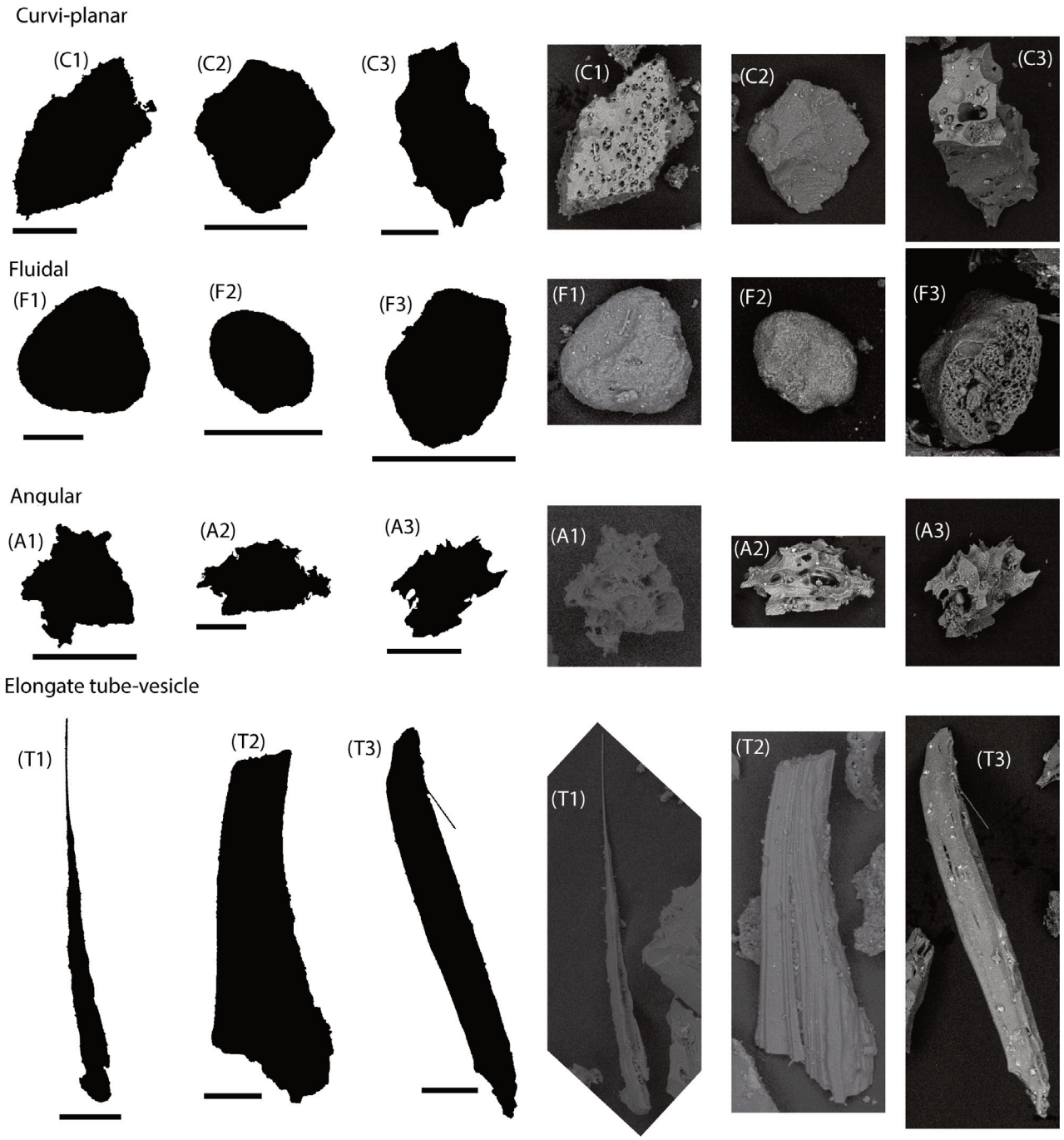

FIGURE 2. Silhouettes of Havre particles used for PARTISAN demonstration run. End members of four morphological classes were used, labelled with "C" (curvi-planar), "F" (fluidal), "A" (angular) and "T" (elongate tube-vesicle). Scale bar is of 100 μm length.

The authors applied this system to investigate basaltic tephra fall samples from six different eruptions with selected grain sizes between 63 and 125 μm: five from Iceland (Fimmvörðuháls 2010, Karl 1210–1240, Katla 1755, Grímsvötn 2011, Hverfjall 2500 BP) and one from Norway (Eggoya 1732), covering different eruptive styles (from Hawaiian to subplinian) and fragmentation mechanisms.

In an effort to morphometrically distinguish phreatomagmatic from magmatic ash grains, the authors developed two main shape parameters: *Feret aspect ratio AF* and *regularity parameter Reg*. The latter is the product of circularity $Circ_{SC}$ multiplied by *rectangularity* Rec_{SC} (equivalent to $Comp_{DL}$) and *form factor* (equivalent to $Circ_{Cl}$), where $Circ_{SC}$ is depending on the bounding circle (see Table 2).

To obtain results consistent with those presented by Schmith et al. [2017], PARTISAN computes the Feret as-

Reference	Location of eruption / source of melt	Composition	fragmentation style inferred by cited authors	Grain size	Imaging method	Remarks
Alvarado et al. [2016]	Turrialba volcano (2010-16), Costa Rica	andesite to dacite	phreatomagmatic / magmatic	88 μm to 125 μm	SEM – silhouette	
Avery et al. [2017]	Taupo, NZ (181 AD Hatepe)	rhyolite	phreatoplinian	0.85 mm to 1.18 mm	SEM - silhouette	
	Redoubt (2009), Alaska	andesite	magmatic	0.6 mm to 1.18 mm	SEM - silhouette	
	Erebus, Antarctica	phonolite	magmatic and phreatomagmatic	0.85 mm to 1.18 mm	SEM - silhouette	
Büttner et al. [2002]	La Fossa, Vulcano (Italy)	shoshonite	phreatomagmatic	≤ 130 μm		
	La Fossa, Vulcano (Italy)	shoshonite	experimental – molten-fuel coolant interaction (MFCI)	≤ 130 μm	SEM - silhouette	
Cannata et al. [2014]	Stromboli volcano, Italy	basalt	Strombolian	<1.4 mm	SEM – slice	
Cioni et al. [2008]	Vesuvius, Italy	phonolite	violent Strombolian	Coarse and fine ash	SEM - silhouette	
Coltelli et al. [2008]	Etna, Italy	basalt	fire fountain	26 μm to 1.122 mm	SEM - silhouette	
Dellino and La Volpe [1996]	Monte Pilato-Rocche Rosse deposits, Lipari	rhyolite	magmatic + phreatomagmatic	Lapilli and 4-5 ϕ (31 μm to 62.5 μm)	macrophotographs (lapilli) SEM silhouette (fine ash)	
Dellino et al. [2005]	Vesuvius, Italy	phonolite to tephri-phonolite	magmatic and phreatomagmatic	200 μm to several cm	Photographs - silhouette	
	Campi Flegrei, Italy	trachyte	phreatomagmatic	200 μm to several cm	Photographs - silhouette	
Dellino et al. [2008]	Vesuvius, Italy	tephri-phonolite	phreatomagmatic	200 μm to several mm	Photographs - silhouette	
	Campi Flegrei, Italy	trachyte	phreatomagmatic	200 μm to several mm	Photographs - silhouette	
Dellino et al. [2012]	Eyjafjallajökull (2010), Iceland	basalt	phreatomagmatic + magmatic	62.5 μm	SEM – silhouette	
Dürig et al. [2012]	Grímsvötn (2004), Iceland	basalt	phreatomagmatic	<125 μm	SEM - silhouette	
	Grímsvötn (2004), Iceland	basalt	experimental – thermal granulation and MFCI	<125 μm	SEM – silhouette	
	Tepexitl, Mexico	rhyolite	phreatomagmatic	<125 μm	SEM – silhouette	
	Tepexitl, Mexico	rhyolite	experimental - thermal granulation, MFCI, and magmatic	<125 μm	SEM – silhouette	
	industrial glass	soda–lime glass	experimental – hammer impact	<125 μm	SEM – silhouette	
Iverson et al. [2014]	Erebus volcano, Antarctica	phonolite	phreatomagmatic to strombolian	10 to 800 μm	SEM – silhouette	

Jordan et al. [2014]	Purrumbete maar, SE Australia	basalt	phreatomagmatic	<125 μm	SEM - silhouette	
	Purrumbete maar, SE Australia	basalt	phreatomagmatic	<125 μm	SEM - silhouette	
Lautze et al. [2012]	Etna (2006), Italy	basalt	magmatic + phreatomagmatic	50-220 μm	SEM – silhouette	
	Stromboli (2007), Italy	basalt	magmatic + phreatomagmatic	50-220 μm	SEM – silhouette	
Lautze et al. [2013]	Stromboli (2009), Italy	basalt	magmatic	100-200 μm	SEM - silhouette	
Mele et al. [2011]	Somma-Vesuvius, Italy	phonolite to tephri-phonolite	magmatic + phreatomagmatic	250 μm to several mm	optical microscope + photographs - silhouette	
	Campi Flegrei, Italy	trachyte	phreatomagmatic	500 μm	optical microscope - silhouette	
	Vulcano, Italy	latite	phreatomagmatic	500 μm	optical microscope - silhouette	
Mele et al. [2015]	Campi Flegrei, Italy	Trachyte	phreatomagmatic	200 μm to several mm	optical microscope + photographs - silhouette	juveniles and crystals
Murtagh and White [2013]	Black Point, California	basalt	magmatic + phreatomagmatic	62.5 μm	SEM - silhouette	
Németh [2010]	Western Hungaria	tephrite to phono tephrite	phreatomagmatic	10 to 300 μm	optical microscope, SEM	
Németh and Cronin [2011]	Ambrym Volcano (1913), Vanuatu	trachy-basalt to basaltic trachy-andesite	magmatic to phreatomagmatic	30-300 μm	optical microscope, SEM (silhouette), SEM (slice)	
Németh et al. [2012]	Orakei, Auckland volcanic field, New Zealand	basalt	phreatomagmatic	62.5 μm to 4 mm	SEM - silhouette	
Schipper [2009]	Lo'ihi Seamount, Hawaii	basalt	phreatomagmatic + magmatic	< 125 μm	SEM - silhouette	
Schipper et al. [2013]	Lo'ihi Seamount, Hawaii	basalt	phreatomagmatic	< 125 μm	SEM - silhouette	
	Lo'ihi Seamount, Hawaii	basalt	experimental – thermal granulation	< 125 μm	SEM - silhouette	
Sulpizio et al. [2010]	Somma-Vesuvius, Italy	tephri-phonolite	phreatomagmatic	200 μm to several mm	optical microscope + photographs - silhouette	
Taddeucci and Palladino [2002]	Latera Volcanic Complex, Italy	trachytic to phonolitic	magmatic	> 0.5 mm	SEM - silhouette	

TABLE 3. List of published studies using IPA parameters for quantitative morphometric analyses.

pect ratio presented in their Figure 3, here denoted AR_{SC}, which is defined as the reciprocal value of A_F.

5. OPERATION METHODS OF PARTISAN

5.1 REQUIREMENTS

PARTISAN runs with the standard version of MATLAB™ and requires the MATLAB™ Image Processing toolbox. To install PARTISAN, the file 'PARTISAN.zip' provided in Supplement S1 has simply to be extracted into a folder of the user's choice.

As input, PARTISAN requires black and white (i.e., binary) images, e.g. of a single clast projected to the XY-plane as a silhouette (see Figure 2) or of a particle cross-section. Lossless formats such as TIFF, BMP or PNG are preferred over lossy formats such as JPEG.

A limitation is that the program does not allow automatic segmentation of images with multiple particles. Each image should show a single particle, with all images placed in the same folder. PARTISAN can then batch analyze all images as a single image stack.

Once the working folder has been assigned, the program can be executed. A step by step instruction can be found in the companion text file 'ReadMe.txt', which is provided with the 'PARTISAN.zip' package (Supplement S1).

5.2 WORKFLOW AND OUTPUT

After being initiated PARTISAN will proceed to cycle through all the matching image files in the assigned directory, processing each of them in turn and collecting the results of the analysis into a common comma-separated text file, ready for opening as a spreadsheet.

Either true-binary (0 or 1) or 8-bit (0 or 255) images may be used. If an image is inverted, this is automatically handled. If an 8-bit grey-scale image contains values other than 0 and 255 it will automatically be thresholded up or down from the central value of 127. Similarly, if a 0 or 1 "binary" image contains floating point values these will be thresholded up or down from 0.5. For details on the algorithms used for measuring the basic parameters (such as perimeter), we refer the reader to comments in the source code including links to further documentation.

During testing, analysis took approximately 1 second per image on a standard desktop PC. If figure generation is enabled, the program will take approximately 75% more time to run. Larger images (larger image files) will take proportionally longer to process.

PARTISAN provides the following output:

- A comma separated .csv ASCII spreadsheet containing all derived parameters, grouped by the name of the authors that first introduced them, is written to a file named 'particle_stats_output.csv' in the current directory. Each row contains the shape parameters for each image, as described in Tables 1 and 2.
- A summary of the parameters is displayed to the MATLAB console as the program runs.
- A figure window is generated for each image, consisting of four plots (see Figure 1): (a) the raw image; (b) the particle rotated to the longer axis of the minimum bounding box; (c) the particle rotated to the maximum Feret distance; and (d) the particle rotated to the major axis of the best-fit ellipse.

These figures are well suited for quality assurance, but should be disabled when bulk processing many images (see 'ReadMe.txt' file in Supplement S1 for more details).

5.3 STRENGTHS AND CAVEATS

Based on comparisons of test data comprising 32 different shapes, PARTISAN is verified to give – with negligible variations in the perimeter – identical output for the IPA parameters as when using the software OptiLab employed by Dellino and La Volpe [1996]. Moreover, all SEM images kept in the archives, named by the authors that first introduced the shape parameters group, have now been reprocessed with PARTISAN, so users of this program can be sure that their results are compatible with those by the groups represented by the authors of the original paper.

As a general rule, due to the reasons mentioned in Section 2, we strongly encourage to make sure that identical imaging and sampling protocols (including imaging type, image resolution, sampling methods, studied grain size) are used as applied to the data sets with which the new datasets will be compared. For example, for obtaining IPA parameters comparable to those kept in the archives by the authors, the area of the cross-section or silhouette (A) should have at least 5000 pixels [Dellino and La Volpe, 1996; Mele et al., 2011; Dürig et al., 2012]. Importantly, empirical studies by Liu et al. [2015a] indicate that under no circumstance should the cross-sectional (or silhouette) area of a particle be smaller than 750 pixels.

PARTISAN can be applied to any type of particle im-

ages so long as minimum pixels-per-particle scaling is kept consistent. It is not appropriate, however, for data from particle shape silhouettes, whether based on SEM images, microtomography, or other light sources, to be directly compared to images of physically sectioned particles.

The program was developed to extract information needed to calculate IPA parameters in the first place, but it also provides a wide range of other data. These can be utilized to calculate parameters used by other authors, allowing comparison of results across methods. Because of differences in image acquisition (resolution, sharpness, pixel thresholds, etc.), comparisons of data from other studies with PARTISAN-extracted equivalents may, however, be imprecise unless original particle images are available to be reprocessed. To ensure best comparability of data in publications we therefore encourage authors to provide not only the values of the resulting shape parameters but also the binary images used as input.

We also want to stress that the measurement even of basic metrics such as perimeter (and partly also other parameters, such as area) depends on the algorithm implemented in the software, as well as image resolution and relative scaling of pixels vs. particle-surface topography. Differences in algorithm may lead to differences in shape parameters provided by PARTISAN versus those provided by commercial software used for the automated morphometric analysis systems. The output for these systems can therefore not be expected to provide directly comparable shape parameter results. We do not have access to these systems, and thus could not test comparability.

To overcome these difficulties we suggest that, whenever possible, binary images from automated image analyzers be stored. This will allow comparisons to be made with results from other image-acquisition and measurement systems now and in the future.

6. DEMONSTRATION: SHAPE ANALYSIS OF SELECTED ASH GRAINS FROM THE HAVRE 2012 SUBMARINE RHYOLITE ERUPTION

In order to demonstrate the functionality of PARTISAN we present results for ash grains collected from deposits of the 2012 submarine Havre eruption, and selected to exemplify the different shapes of clasts in the ash.

6.1 GEOLOGICAL BACKGROUND

Havre is a seamount volcano located along the Kermadec arc with its base at 1500-2000 meters below sea level [Wright et al., 2006] and a post-2012 peak along the caldera wall at 600 mbsl. The caldera is 3x4 km elongated toward NW-SW, with average caldera-rim depth of 900 m [Wright et al., 2006] and mostly flat caldera floor at 1500 mbsl.

In 2012 Havre volcano erupted, with a satellite image at 10:50 18th July 2012 UTC showing an atmospheric plume, a 400 km^2 area of pumice raft on the sea and a plume of discoloured, ash-stained, water emanating from a hot spot point source above Havre. After 21st July 2012 no further activity at Havre was detected. The eruption produced 14 lava flows from 11 vents along the southern caldera rim and the southwest caldera wall [Carey et al., 2018] and three seafloor clastic deposits, all of which were described, sampled and mapped at high resolution during a 2015 cruise using the autonomous underwater vehicle (AUV) Sentry and the remotely operated vehicle (ROV) Jason. The seafloor clastic deposit of interest here includes an ash-dominant unit termed the Ash with Lapilli (AL). It extends across the whole of the caldera floor and shoulders, showing no clear grainsize or thinning trends to the limits of the 2015 investigation area.

Ash from the AL was sampled from locations around the summit and caldera of Havre volcano using ROV Jason [Murch et al., 2018]. Because the Havre ash is very fine-grained (many samples have a modal particle size of 16-32 µm) it is critical to separate different simple shapes. Also, on these very small particles, effects of surface irregularities are subdued compared with such effects for larger volcanic grains. Havre ash particles were thus divided into 4 morphological classes based on their key shape characteristics (see Figure 2): curvi-planar (labelled “C”), angular (“A”), fluidal (“F”), and elongate tube-vesicle (“T”) [Murch et al., 2018]. Curvi-planar clasts are defined by planar and curvi-planar surfaces that intersect to form sharp edges and include both platy and subequant blocky clasts. Vesicles in curvi-planar clasts are cross-cut by fracture surfaces, which show no deformation around the bubble. Angular clasts have prominent concavities defined by brittle-fractured vesicle walls. Fluidal clasts have exterior features indicating surface-tension or fluid-dynamic reshaping of the grains while molten. Fluidal clasts include both those with a wholly fluidal form, and those that preserve a single fluidal surface. Fluidal particles are commonly crosscut by un-deformed curvi-planar fracture surfaces. Elongate

system	shape parameters	A1	A2	A3	C1	C2	C3	F1	F2	F3	T1	T2	T3
Dellino and La Volpe [1996]	$Circ_{DL}$	1.53	2.09	1.95	1.65	1.22	1.43	1.13	1.11	1.20	3.52	1.61	2.34
	Rec_{DL}	1.10	1.41	1.40	1.15	0.97	1.03	0.88	0.85	0.91	1.07	0.98	1.12
	Com_{DL}	0.66	0.64	0.69	0.66	0.80	0.73	0.76	0.77	0.76	0.41	0.61	0.63
	Elo_{DL}	1.46	2.51	1.89	2.66	1.23	2.37	1.33	1.72	1.76	24.22	4.73	9.89
Cioni et al. [2014]	$Circ_{Cl}$	0.42	0.23	0.26	0.37	0.67	0.49	0.78	0.82	0.70	0.08	0.38	0.18
	AR_{Cl}	1.05	1.69	1.45	1.77	1.14	1.94	1.06	1.29	1.40	12.72	3.65	8.21
	Con_{Cl}	0.82	0.62	0.65	0.74	0.92	0.87	0.99	0.97	0.92	1.11	1.02	0.92
	Sol_{Cl}	0.82	0.84	0.82	0.89	0.95	0.88	0.98	0.97	0.96	0.60	0.81	0.82
Leibrandt and Le Pennec [2015]	$Circ_{LL}$	0.65	0.48	0.51	0.60	0.82	0.70	0.88	0.90	0.84	0.28	0.62	0.43
	Elo_{LL}	0.10	0.44	0.33	0.43	0.08	0.46	0.06	0.23	0.26	0.92	0.66	0.85
	AR_{LL}	0.90	0.56	0.67	0.57	0.92	0.54	0.94	0.77	0.74	0.08	0.34	0.15
	d_{-H}	121	251	211	286	228	309	198	122	200	207	331	355
	Con_{LL}	0.80	0.60	0.63	0.74	0.91	0.87	0.95	0.98	0.93	0.90	0.93	0.86
	Sol_{LL}	0.82	0.84	0.82	0.89	0.95	0.88	0.98	0.97	0.96	0.60	0.81	0.82
Liu et al. [2015]	FF	0.42	0.23	0.26	0.37	0.67	0.49	0.78	0.82	0.70	0.08	0.38	0.18
	AR_{LI}	0.96	0.59	0.69	0.56	0.88	0.52	0.94	0.77	0.72	0.08	0.27	0.12
	Con_{LI}	0.80	0.60	0.63	0.74	0.91	0.87	0.95	0.98	0.93	0.90	0.93	0.86
	Sol_{LI}	0.82	0.84	0.82	0.89	0.95	0.88	0.98	0.97	0.96	0.60	0.81	0.82
Schmith et al. [2017]	$Circ_{SC}$	0.61	0.43	0.54	0.47	0.74	0.46	0.81	0.74	0.69	0.04	0.26	0.12
	Rec_{SC}	0.66	0.64	0.69	0.66	0.80	0.73	0.76	0.77	0.76	0.41	0.61	0.63
	FF	0.42	0.23	0.26	0.37	0.67	0.49	0.78	0.82	0.70	0.08	0.38	0.18
	AR_{SC}	1.12	1.87	1.46	1.79	1.01	1.86	1.03	1.32	1.34	11.84	2.93	6.49
	Reg	0.17	0.06	0.10	0.11	0.40	0.16	0.48	0.47	0.37	0.00	0.06	0.01

TABLE 4. Output results by PARTISAN for the particle shapes displayed in Figure 2. The complete output file labelled "particle_stats_output.csv" can be found in Supplement S3.

tube-vesicle clasts are bounded by either fluidal or brittle fracture surfaces but typically show curvi-planar fractures that run perpendicular to the elongation direction at either end of the grain.

6.2 DEMONSTRATION OF RESULTS GIVEN BY PARTISAN

In Figure 2, binarized projections of end-member examples of each morphology class are shown. These images are provided in Supplement S2 and can be used by the reader to practice applying the script. The relevant output results for these particle silhouettes, following the five shape parameterization approaches, are shown in Table 4. The complete output can be found in Supplement S3.

For this demonstration, imagine that these test data represent a large set of imaged grains, which we want to statistically analyze for features indicative of fragmentation style. Particle-shape analysis and PARTISAN will help us to explore and find the best morphometric system to discriminate between grains generated by brittle versus ductile fragmentation mechanisms. If applied to representative sample populations, such a procedure could provide a smart way to automate particle classification for statistical analysis, which otherwise would take tedious hours of manual sorting.

While curvi-planar and angular particles of the classes "A" and "C" can be assigned to brittle generation processes, the second group includes, in addition to the – descriptively named – fluidal grains (class "F"), also the elongate tube-vesicle (class "T") clasts, which were shaped by ductile stretching.

Our aim in this example is to find shape parameters which can be plotted against one another, individually or in combination, to provide the best discrimination between brittle and ductile particles. For this purpose we utilize and compare existing diagrams as proposed by various studies for each morphometric system implemented in PARTISAN (see Figure 3).

Figure 3(a) follows the IPA system as defined by Dellino and La Volpe [1996] showing the plot of Rec_{DL} x Com_{DL} vs Elo_{DL} x $Circ_{DL}$. This type of diagram has also been used for example by Büttner et al. [2002] to define a morphometric boundary (green dashed line) to discriminate shoshonite clasts by shape between brittle and ductile fragmentation mechanisms. For the rhyolitic grains demonstrated here the brittle-ductile (brittle-fluid) boundary appears to be lower on the y-axis (blue dashed line). The IPA plot has correctly placed the elongate tubular-vesicle clasts of class "T" in the ductile field, together with the fluidal grains of class "F", despite their very different overall shapes.

In Figure 3(b) another kind of IPA diagram is displayed, after Murtagh and White [2013]. A line separating "F" and "T" particles from "C" and "A" ones is possible (solid line), but the location is slightly different from their boundary (dashed line), and the F and T grains lie in their 'phreatomagmatic' field (because the other field captures vesicular fragments, hence the C and A grains). We do not recommend the use of this diagram for fine rhyolite ash.

Figure 3(c) shows the Havre results plotted following Cioni et al. [2014], who used their plot to discriminate ash from phreatomagmatic versus magmatic phases of the Eyjafjallajökull 2010 eruption. In our example, this diagram does not discriminate well the two groups of fragmentation mechanisms, since "T" and "F" class data points plot in significantly different sectors of the plot, which makes it difficult to group them together. The "F" and "A" class particles plot close together, whereas C class particles appear to cover a larger range in the diagram, which makes it difficult to achieve the desired discrimination.

In Figure 3(d) the Havre data are plotted in a diagram proposed by Leibrandt and Le Pennec [2015], using their morphometric system to discriminate between eruptive styles in ongoing eruptions. While "C" and "A" class data intersect, the data points for "T" class grains are plotted in a different area. The "F" class data points, however, are separated from the T' class data with "C" class data interfering, which inhibits the definition of a simple discrimination criterion that would separate grains formed in 'brittle' versus 'ductile' regimes.

Figure 3(e) displays the data of the Havre samples in a diagram type suggested by Liu et al. [2015a]. Our results are, however, based on particle silhouettes, which are not expected to match with slices as used by [Liu et al., 2015a, 2015b, 2017]. The 'A' and "C" class data plot with broad scatter, making it difficult to discriminate them from the "T" and "F" grains.

Figures 3 (f) plots the test data into a diagram provided by Schmith et al. [2017], in which the regularity parameter *Reg* is plotted over the Feret aspect ratio AR_{SC}. This type of diagram can be used to derive a parameter introduced as *regularity index* (defined as the slope of the linear trendline), which was found to be sensitive to fragmentation style [Schmith et al., 2017]. We note that in contrast to the original diagram by these authors we use a larger range for the AR_{SC} -axis, in order to be able to display all of our data points. In good agreement to Schmith et al. [2017] the "T" class data points all plot to the right of the dashed line, which indicates the threshold between elongated and non-elongated particles as found in their study. The overlap of "C" and "F" class

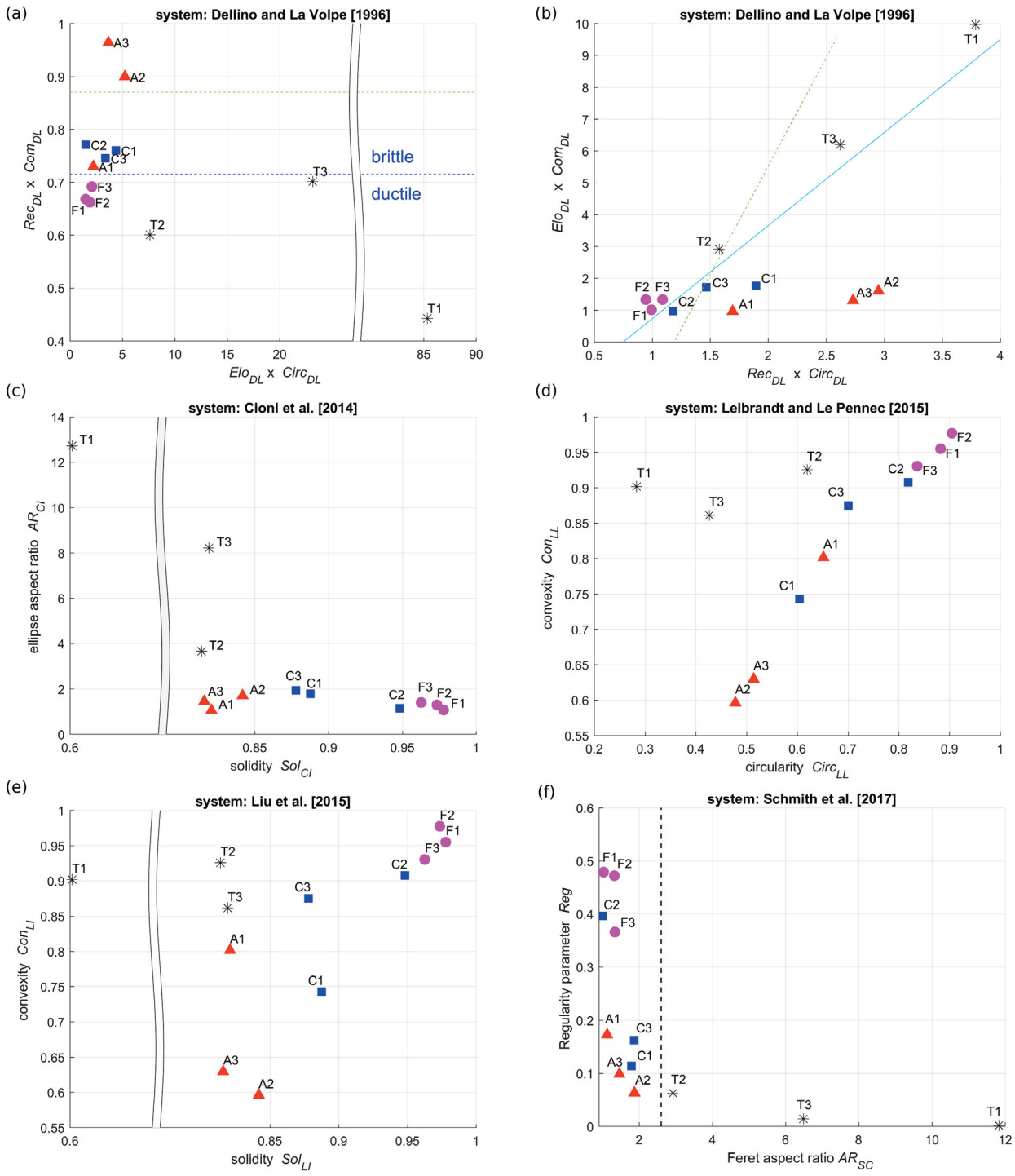

FIGURE 3. Morphometric diagrams as used in morphometric systems underlying PARTISAN. (a) Image particle shape analysis diagram using the system by Dellino and La Volpe [1996]. Green dashed line indicates boundary between brittle and ductile fragmentation regime provided by Büttner et al. [2002] for shoshonite clasts. In contrast, the shape of rhyolitic Havre particles with brittle angular and curvi-planar features suggest a lowered boundary (blue line). (b) Complementary IPA diagram with axes as used by, e.g., Murtagh and White [2013]. In addition, the resulting diagrams according to the presentation methods by Cioni et al. [2014] (c), Leibrandt and Le Pennec [2015] (d), Liu et al. [2015a] (e) and Schmith et al. [2017] (f) are presented. In the latter plot the dashed line indicates the threshold between elongated and non-elongated particles as found by Schmith et al. [2017]. For the analyzed Havre ash particles, the best choice for an automated discrimination between brittle and ductile particle classes would be the morphometric system and diagram type presented in (a).

data, however, do not support use of this system for establishing a 'brittle/ductile' discrimination criterion.

For each system, the results followed the expected trends with fluidal particles appearing more circular, an-

gular particles plotting as more irregular, and curvi-planar particles generally falling between these two clusters. The elongate tube-vesicle clasts are characterized by extreme elongation parameters, such as the aspect ratio.

For our objective in this demonstration, the discrimination of brittle-fragmented from ductile-fragmented clasts, the IPA system shown in Figure 3(a) is the best of the six compared.

The small number of selected particles with 'extreme' shapes used in this demonstration are not considered to be representative of the overall Havre eruption. The findings also are insufficient to support general advice on which morphometric system is best to use for achieving various volcanological goals. This choice must be made by the users, based on the aims of shape analysis in different projects. Existing data sets and their comparability in terms of sample type, grain size, and particle imaging method should be considered. What PARTISAN provides is a holistic tool for selecting and using the best fitting morphometric systems and diagrams.

7. CONCLUSIONS

PARTISAN is a Free and Open Source software (FOSS) routine that runs in MATLAB to parameterize 2D shapes of particle silhouettes and provide IPA statistics [Dellino and La Volpe, 1996]. It also extracts other parameters that can, with some unavoidable caveats, allow cross-comparisons among other 2D morphological routines. The same parameters for external 2D shape can be measured for both silhouettes and sectioned particles, but shapes of particles prepared in these different ways cannot be compared directly. With a test case using ash grains from a submarine rhyolite eruption we demonstrated how PARTISAN can be used to find the most suitable shape analysis method for a specific task.

Data and sharing resources

- Supplement S1: PARTISAN.zip, containing the files Partisan.m, minBoundCircle.m, minBoundEllipse.m, minBoundingBox.m and cog_coord.m
- Supplement S2: clasts.zip, containing 12 .tif images of particle silhouettes
- Supplement S3: particle_stats_output.csv, demonstration output file provided by PARTISAN

Acknowledgements. This study was supported by a MARSDEN grant (U001616 to JW), and Havre samples were obtained with funding from NSF (EAR1447559 to JW). John D'Errico, Julien Diener and Anye Li and are gratefully acknowledged for providing useful open source MATLAB functions, which have been integrated into PARTISAN. Julie Haas is gratefully acknowledged for the BreakXAxis plot function used in this paper. Many thanks go to Erin Todd and Louise Steffensen Schmidt for helpful discussions. Furthermore we would like to express our gratitude to the editor Fabio Dioguardi and to Pierre-Simon Ross and Johanne Schmith for their thoughtful and constructive comments which helped us to improve the quality of our paper.

REFERENCES

Alvarado, G. E., Mele, D., Dellino, P., de Moor, J. M., and Avard, G. (2016). Are the ashes from the latest eruptions (2010–2016) at Turrialba volcano (Costa Rica) related to phreatic or phreatomagmatic events? Journal of Volcanology and Geothermal Research 327, 407–415. doi:10.1016/j.jvolgeores.2016.09.003.

Avery, M. R., Panter, K. S., and Gorsevski, P. V. (2017). Distinguishing styles of explosive eruptions at Erebus, Redoubt and Taupo volcanoes using multivariate analysis of ash morphometrics. Journal of Volcanology and Geothermal Research 332, 1–13. doi:10.1016/j.jvolgeores.2017.01.010.

Büttner, R., Dellino, P., and Zimanowski, B. (1999). Identifying magma-water interaction from the surface features of ash particles. Nature; London 401, 688–690. doi:http://dx.doi.org.ezproxy.otago-.ac.nz/10.1038/44364.

Büttner, R., Dellino, P., La Volpe, L., Lorenz, V., and Zimanowski, B. (2002). Thermohydraulic explosions in phreatomagmatic eruptions as evidenced by the comparison between pyroclasts and products from Molten Fuel Coolant Interaction experiments. J. Geophys. Res. 107, 2277. doi:10.1029-/2001JB000511.

Cannata, C. B., Rosa, R. D., Donato, P., and Taddeucci, J. (2014). Ash Features from Ordinary Activity at Stromboli Volcano. International Journal of Geosciences 05, 1361–1382. doi:10.4236/-ijg.2014.511111.

Carey, R., Soule, S. A., Manga, M., White, J., Mcphie, J., Wysoczanski, R., et al. (2018). The largest deep ocean silicic volcanic eruption of the past century.

Science Advances, 1–7.

Cioni, R., Sbrana, A., and Vecci, R. (1992). Morphologic features of juvenile pyroclasts from magmatic and phreatomagmatic deposits of Vesuvius. Journal of Volcanology and Geothermal Research 51, 61–78.

Cioni, R., D'Oriano, C., and Bertagnini, A. (2008). Fingerprinting ash deposits of small scale eruptions by their physical and textural features. Journal of Volcanology and Geothermal Research 177, 277–287. doi:10.1016/j.jvolgeores.2008.06.003.

Cioni, R., Pistolesi, M., Bertagnini, A., Bonadonna, C., Hoskuldsson, A., and Scateni, B. (2014). Insights into the dynamics and evolution of the 2010 Eyjafjallajökull summit eruption (Iceland) provided by volcanic ash textures. Earth and Planetary Science Letters 394, 111–123. doi:10.1016/-j.epsl.2014.02.051.

Coltelli, M., Miraglia, L., and Scollo, S. (2008). Characterization of shape and terminal velocity of tephra particles erupted during the 2002 eruption of Etna volcano, Italy. Bulletin of Volcanology 70, 1103–1112. doi:10.1007/s00445-007-0192-8.

Dellino, P., and La Volpe, L. (1996). Image processing analysis in reconstructing fragmentation and transportation mechanisms of pyroclastic deposits. The case of Monte Pilato-Rocche Rosse eruptions, Lipari (Aeolian islands, Italy). Journal of Volcanology and Geothermal Research 71, 13–29. doi:10.1016/0377-0273(95)00062-3.

Dellino, P., La Volpe, L., Isaia, R., and Orsi, G. (2001). Statistical analysis of textural data from complex pyroclastic sequences: implications for fragmentation processes of the Agnano-Monte Spina Tephra (4.1 ka), Phlegraean Fields, southern Italy. Bulletin of Volcanology 63, 443–461. doi:10.1007/s004450100163.

Dellino, P., Mele, D., Bonasia, R., Braia, G., La Volpe, L., and Sulpizio, R. (2005). The analysis of the influence of pumice shape on its terminal velocity. Geophysical Research Letters 32. doi:10.1029/2005GL023954.

Dellino, P., Mele, D., Sulpizio, R., La Volpe, L., and Braia, G. (2008). A method for the calculation of the impact parameters of dilute pyroclastic density currents based on deposit particle characteristics. Journal of Geophysical Research 113. doi:10.1029/2007JB005365.

Dellino, P., Gudmundsson, M. T., Larsen, G., Mele, D., Stevenson, J. A., Thordarson, T., et al. (2012). Ash from the Eyjafjallajökull eruption (Iceland): Fragmentation processes and aerodynamic behavior: EYJAFJALLAJÖKULL ERUPTION ASH. Journal of Geophysical Research: Solid Earth 117. doi:10.1029/2011JB008726.

Durant, A. J., Rose, W. I., Sarna-Wojcicki, A. M., Carey, S., and Volentik, A. C. M. (2009). Hydrometeor-enhanced tephra sedimentation: Constraints from the 18 May 1980 eruption of Mount St. Helens. Journal of Geophysical Research 114. doi:10.1029/2008JB005756.

Dürig, T., Mele, D., Dellino, P., and Zimanowski, B. (2012). Comparative analyses of glass fragments from brittle fracture experiments and volcanic ash particles. Bull Volcanol 74, 691–704. doi:10.1007/s00445-011-0562-0.

Eychenne, J., Houghton, B. F., Swanson, D. A., Carey, R. J., and Swavely, L. (2015). Dynamics of an open basaltic magma system: The 2008 activity of the Halema'uma'u Overlook vent, K□lauea Caldera. Earth and Planetary Science Letters 409, 49–60. doi:10.1016/j.epsl.2014.10.045.

Gurioli, L., Andronico, D., Bachelery, P., Balcone-Boissard, H., Battaglia, J., Boudon, G., et al. (2015). MeMoVolc consensual document: a review of cross-disciplinary approaches to characterizing small explosive magmatic eruptions. Bulletin of Volcanology 77. doi:10.1007/s00445-015-0935-x.

Heiken, G. (1972). Morphology and petrography of volcanic ashes. Geological Society of America Bulletin 83, 1961–1988.

Heiken, G. (1974). Atlas of Volcanic Ash. Smithsonian Contributions to the Earth Sciences, 1–101. doi:10.5479/si.00810274.12.1.

Heiken, G., and Wohletz, K. (1985). Volcanic ash. Berkeley: University of California Press.

Iverson, N. A., Kyle, P. R., Dunbar, N. W., McIntosh, W. C., and Pearce, N. J. G. (2014). Eruptive history and magmatic stability of Erebus volcano, Antarctica: Insights from englacial tephra. Geochemistry, Geophysics, Geosystems 15, 4180–4202. doi:10.1002/2014GC005435.

Jordan, S. C., Dürig, T., Cas, R. A. F., and Zimanowski, B. (2014). Processes controlling the shape of ash particles: Results of statistical IPA. Journal of Volcanology and Geothermal Research 288, 19–27. doi:10.1016/j.jvolgeores.2014.09.012.

Klawonn, M., Frazer, L. N., Wolfe, C. J., Houghton, B. F., and Rosenberg, M. D. (2014). Constraining par-

ticle size-dependent plume sedimentation from the 17 June 1996 eruption of Ruapehu Volcano, New Zealand, using geophysical inversions. Journal of Geophysical Research: Solid Earth 119, 1749–1763. doi:10.1002/2013JB010387.

Lautze, N. C., Taddeucci, J., Andronico, D., Cannata, C., Tornetta, L., Scarlato, P., et al. (2012). SEM-based methods for the analysis of basaltic ash from weak explosive activity at Etna in 2006 and the 2007 eruptive crisis at Stromboli. Physics and Chemistry of the Earth, Parts A/B/C 45–46, 113–127. doi:10.1016/j.pce.2011.02.001.

Lautze, N., Taddeucci, J., Andronico, D., Houghton, B., Niemeijer, A., and Scarlato, P. (2013). Insights into explosion dynamics and the production of ash at Stromboli from samples collected in real-time, October 2009. Geological Society of America Special Papers 498, 125–139.

Leibrandt, S., and Le Pennec, J.-L. (2015). Towards fast and routine analyses of volcanic ash morphometry for eruption surveillance applications. Journal of Volcanology and Geothermal Research 297, 11–27. doi:10.1016/j.jvolgeores.2015.03.014.

Liu, E. J., Cashman, K. V., and Rust, A. C. (2015a). Optimising shape analysis to quantify volcanic ash morphology. GeoResJ 8, 14–30. doi:10.-1016/j.grj.2015.09.001.

Liu, E. J., Cashman, K. V., Rust, A. C., and Gislason, S. R. (2015b). The role of bubbles in generating fine ash during hydromagmatic eruptions. Geology 43, 239–242. doi:10.1130/G36336.1.

Liu, E. J., Cashman, K. V., Rust, A. C., and Höskuldsson, A. (2017). Contrasting mechanisms of magma fragmentation during coeval magmatic and hydromagmatic activity: the Hverfjall Fires fissure eruption, Iceland. Bulletin of Volcanology 79. doi:10.1007/s00445-017-1150-8.

Mele, D., Dellino, P., Sulpizio, R., and Braia, G. (2011). A systematic investigation on the aerodynamics of ash particles. Journal of Volcanology and Geothermal Research 203, 1–11. doi:10.1016-/j.jvolgeores.2011.04.004.

Mele, D., Dioguardi, F., Dellino, P., Isaia, R., Sulpizio, R., and Braia, G. (2015). Hazard of pyroclastic density currents at the Campi Flegrei Caldera (Southern Italy) as deduced from the combined use of facies architecture, physical modeling and statistics of the impact parameters. Journal of Volcanology and Geothermal Research 299, 35–53. doi:10.1016/j.jvolgeores.2015.04.002.

Miwa, T., Geshi, N., and Shinohara, H. (2013). Temporal variation in volcanic ash texture during a vulcanian eruption at the Sakurajima volcano, Japan. Journal of Volcanology and Geothermal Research 260, 80–89. doi:10.1016/j.jvolgeores.2013.05.010.

Miwa, T., Shimano, T., and Nishimura, T. (2015). Characterization of the luminance and shape of ash particles at Sakurajima volcano, Japan, using CCD camera images. Bulletin of Volcanology 77. doi:10.1007/s00445-014-0886-7.

Murch, A., White, J. D. L., and Carey, R. J. (2018). Characteristics and deposit stratigraphy of submarine-erupted silicic ash, Havre volcano, Kermadec Arc, New Zealand. Frontiers in Earth Science, accepted.

Murtagh, R. M., and White, J. D. L. (2013). Pyroclast characteristics of a subaqueous to emergent Surtseyan eruption, Black Point volcano, California. Journal of Volcanology and Geothermal Research 267, 75–91. doi:10.1016/j.jvolgeores.2013.08.015.

Németh, K. (2010). "Monogenetic volcanic fields: Origin, sedimentary record, and relationship with polygenetic volcanism," in Geological Society of America Special Papers (Geological Society of America), 43–66. doi:10.1130/2010.2470(04).

Németh, K., and Cronin, S. J. (2011). Drivers of explosivity and elevated hazard in basaltic fissure eruptions: the 1913 eruption of Ambrym Volcano, Vanuatu (SW-Pacific). Journal of volcanology and geothermal research 201, 194–209.

Németh, K., Cronin, S. J., Smith, I. E., and Flores, J. A. (2012). Amplified hazard of small-volume monogenetic eruptions due to environmental controls, Orakei Basin, Auckland Volcanic Field, New Zealand. Bulletin of volcanology 74, 2121–2137.

Riley, C. M., Rose, W. I., and Bluth, G. J. S. (2003). Quantitative shape measurements of distal volcanic ash: QUANTITATIVE SHAPE MEASUREMENTS OF ASH. Journal of Geophysical Research: Solid Earth 108. doi:10.1029/2001JB000818.

Schipper, C. I. (2009). Explosive Submarine Volcanism at L□ihi Seamount, Hawaii. PhD thesis, Geology Department, University of Otago, 199p.

Schipper, C. I., Sonder, I., Schmid, A., White, J. D. L., Dürig, T., Zimanowski, B., et al. (2013). Vapour dynamics during magma–water interaction experiments: hydromagmatic origins of submarine volcaniclastic particles (limu o Pele). Geophys J Int 192, 1109–1115. doi:10.1093/gji/ggs099.

Schmith, J., Höskuldsson, Á., and Holm, P. M. (2017). Grain shape of basaltic ash populations: implications for fragmentation. Bulletin of Volcanology 79. doi:10.1007/s00445-016-1093-5.

Schneider, C. A., Rasband, W. S., and Eliceiri, K. W. (2012). NIH Image to ImageJ: 25 years of image analysis. Nature Methods 9, 671–675. doi:10.1038/nmeth.2089.

Sulpizio, R., Bonasia, R., Dellino, P., Mele, D., Di Vito, M. A., and La Volpe, L. (2010). The Pomici di Avellino eruption of Somma–Vesuvius (3.9 ka BP). Part II: sedimentology and physical volcanology of pyroclastic density current deposits. Bulletin of Volcanology 72, 559–577. doi:10.1007/s00445-009-0340-4.

Suzuki, Y., Nagai, M., Maeno, F., Yasuda, A., Hokanishi, N., Shimano, T., et al. (2013). Precursory activity and evolution of the 2011 eruption of Shinmoe-dake in Kirishima volcano—insights from ash samples. Earth, Planets and Space 65, 591–607. doi:10.5047/eps.2013.02.004.

Taddeucci, J., and Palladino, D. (2002). Particle size-density relationships in pyroclastic deposits: inferences for emplacement processes. Bulletin of Volcanology 64, 273–284. doi:10.1007/s00445-002-0205-6.

Wright, I. C., Worthington, T. J., and Gamble, J. A. (2006). New multibeam mapping and geochemistry of the 30°-35° S sector, and overview, of southern Kermadec arc volcanism. Journal of Volcanology and Geothermal Research 149, 263–296. doi:10.1016/j.jvolgeores.2005.03.021.

Wright, H. M. N., Cashman, K. V., Mothes, P. A., Hall, M. L., Ruiz, A. G., and Le Pennec, J.-L. (2012). Estimating rates of decompression from textures of erupted ash particles produced by 1999-2006 eruptions of Tungurahua volcano, Ecuador. Geology 40, 619–622. doi:10.1130/G32948.1.

Yamanoi, Y., Takeuchi, S., Okumura, S., Nakashima, S., and Yokoyama, T. (2008). Color measurements of volcanic ash deposits from three different styles of summit activity at Sakurajima volcano, Japan: Conduit processes recorded in color of volcanic ash. Journal of Volcanology and Geothermal Research 178, 81–93. doi:10.1016/j.jvolgeores.2007.11.013.

*CORRESPONDING AUTHOR: Tobias DÜRIG,
Geology Department, University of Otago
University of Otago,
Dunedin, New Zealand
email: tobias.durig@otago.ac.nz